Chemical Engineering Journal 547 (2026) 180726

Contents lists available at ScienceDirect

Chemical Engineering Journal

journal homepage: www.elsevier.com/locate/cej

A phase-matched flexible PVDF ultrasonic transducer for efficiently powering implantable bioelectronics

Jinlong Sun [a], Boling Lan [a], Shenglong Wang [a], Hongguang Li [a], Tianpei Xu [a], Longchao Huang [a], Peiwen Li [a], Wei Zhao [a], Yong Ao [a], Long Jin [a], Wei Zhu [c,*], Weiqing Yang [a,b], Weili Deng [a,*]

[a] Key Laboratory of Advanced Technologies of Materials (Ministry of Education), School of Materials Science and Engineering, Southwest Jiaotong University, Chengdu, Sichuan, 610031, PR China
[b] Research Institute of Frontier Science, Southwest Jiaotong University, Chengdu, Sichuan 610031, PR China
[c] School of Energy and Power Engineering, Nanjing University of Science and Technology, Nanjing, 210094, PR China

ARTICLE INFO

Keywords:
Phase matching
PVDF
Ultrasonic transducer
Energy harvesting
Wireless power transfer

ABSTRACT

Securing a continuous and biocompatible power supply remains a primary challenge for implantable devices. Ultrasonic wireless power transfer based on poly(vinylidene fluoride) (PVDF) transducers exhibits excellent acoustic impedance matching with soft tissues. However, insufficient acoustic-to-electric conversion efficiency restricts their practical applications. Here, we propose a vertically stacked ultrasonic energy harvester integrating dual PVDF functional layers. Guided by theoretical acoustic wavelength calculations and multiphysics simulations, the interlayer spacing is rationally engineered to achieve identical phase responses across both functional layers during ultrasonic propagation. This phase-matched architecture enables synchronized acoustic excitation and constructive superposition of piezoelectric potentials across the stacked PVDF layers, thereby maximizing acoustic energy conversion. Evaluated under a weak ultrasonic field, the device delivers an output power of 156.56 μW and a power density of 423.14 μW/cm^3, demonstrating an 89.12% improvement over conventional single-layer devices without compromising intrinsic structural flexibility. Meanwhile, compared with conventional piezoelectric ceramic transducers, the proposed PVDF-based device retains the distinctive advantages of low acoustic impedance, full flexibility, and improved tissue conformability, which are highly desirable for efficient ultrasonic coupling and energy transfer in implantable applications. This phase-matching strategy provides a scalable approach to improve the efficiency of polymer-based piezoelectric harvesters, advancing the development of sustainable power sources for implantable bioelectronics.

1. Introduction

The long-term operation of implantable medical devices (IMDs) critically relies on a continuous and biosafe energy supply [1–7]. The rapid evolution of implantable bioelectronics, including neural prostheses, biosensors, and neurostimulators, imposes stringent requirements on power units regarding miniaturization, durability, stability, and biocompatibility [8–11]. However, conventional batteries are constrained by finite lifespans, bulky footprints, and the necessity for invasive surgical replacement [10,12–15]. While percutaneous wiring bypasses the limitations of energy harvesting and energy storage, it introduces high risks of infection, inflammation, and tissue damage [10,16–19]. Although significant progress has been achieved in harvesting in vivo biomechanical energy [20], the conversion efficiency of such devices remains inherently limited, and their application is strictly confined to anatomical sites, often rendering them difficult to meet practical power demands [21]. Consequently, developing safe and efficient in vivo wireless power transfer (WPT) technologies has emerged as a central challenge in implantable bioelectronics.

Among existing WPT strategies, ultrasound is highly promising for powering deep-tissue implants due to its low tissue attenuation, substantial penetration depth, and excellent spatial focusing [22–26]. Compared with electromagnetic induction and radio-frequency transmission, ultrasound enables superior energy coupling in deep tissues while ensuring biosafety [22]. Current ultrasonic energy harvesters are primarily based on triboelectric and piezoelectric mechanisms [3,27]. Although triboelectric nanogenerators are capable of harvesting acoustic energy, their inherently high internal impedance makes it difficult to

* Corresponding authors.
E-mail addresses: zhuwei@njust.edu.cn (W. Zhu), weili1812@swjtu.edu.cn (W. Deng).

https://doi.org/10.1016/j.cej.2026.180726
Received 9 May 2026; Received in revised form 24 July 2026; Accepted 12 August 2026
Available online 15 August 2026
1385-8947/© 2026 Elsevier B.V. All rights are reserved, including those for text and data mining, AI training, and similar technologies.

achieve efficient matching with external circuits, thereby limiting effective power delivery and restricting their applications [28–34]. In contrast, piezoelectric devices directly convert acoustic pressure into electricity through the piezoelectric effect. Their fast response, stable output, and robust adaptability to ultrasonic excitation make them the mainstream route for ultrasonic energy harvesting [3,33,35,36].

High-performance ultrasonic transducers typically utilize inorganic piezoelectric ceramics. Despite their high piezoelectric coefficients and strong electromechanical coupling [37,38], the toxicity of lead-based ceramics raises severe biosafety concerns [25,39–41]. Furthermore, their rigidity and brittleness prevent conformal attachment and dynamic adaptation in implantable devices [42–45]. Alternatively, piezoelectric polymers like poly(vinylidene fluoride) (PVDF) offer intrinsic flexibility, biocompatibility, and low acoustic impedance [46–51]. These properties facilitate better acoustic matching with soft tissues, thereby minimizing interfacial reflection losses and improving acoustic energy coupling [47,52]. However, the inherently weak piezoelectric response of semicrystalline PVDF results in a significantly lower acoustic-to-electric conversion efficiency than that of piezoceramics [53–56]. Consequently, only a limited portion of the incident ultrasonic energy is converted into usable electrical output, while the remaining energy persists in propagation and is ultimately dissipated. This low energy utilization leads to considerable waste of transmitted ultrasonic energy and thus hampers the further development of PVDF-based flexible ultrasonic transducers. Although incorporating functional fillers, such as MXene or barium titanate, into polymers can effectively improve their intrinsic piezoelectric coefficients [20,43,57], this approach remains fundamentally constrained by a macroscopic physical limitation inherent to single-layer thin films: a substantial portion of the incident ultrasonic energy is transmitted directly through the film and dissipated, rather than being harnessed effectively.

To address this issue, we propose a vertically stacked piezoelectric ultrasonic transducer featuring dual PVDF functional layers (DL-PVDF-PUT). Guided by theoretical acoustic wavelength calculations and multiphysics simulations, we rationally engineered the interlayer spacing to ensure identical phase responses of both PVDF layers during ultrasonic propagation. This phase-matching strategy synchronizes the acoustic excitation across the stacked PVDF layers, leading to in-phase generation and constructive superposition of piezoelectric potentials. In contrast to conventional single-layer PVDF transducers, this dual-layer configuration improves the utilization of incident ultrasonic energy, significantly boosting electrical output without compromising device flexibility. Meanwhile, compared with conventional piezoelectric ceramic transducers, the proposed PVDF-based device retains the distinctive advantages of low acoustic impedance, full flexibility, and improved tissue conformability, which are highly desirable for efficient ultrasonic coupling and energy transfer in implantable applications. Under low-intensity ultrasonic excitation, the fabricated DL-PVDF-PUT achieves an output power of 156.56 μW and a power density of 423.14 μW/cm^3, representing an 89.12% enhancement over its single-

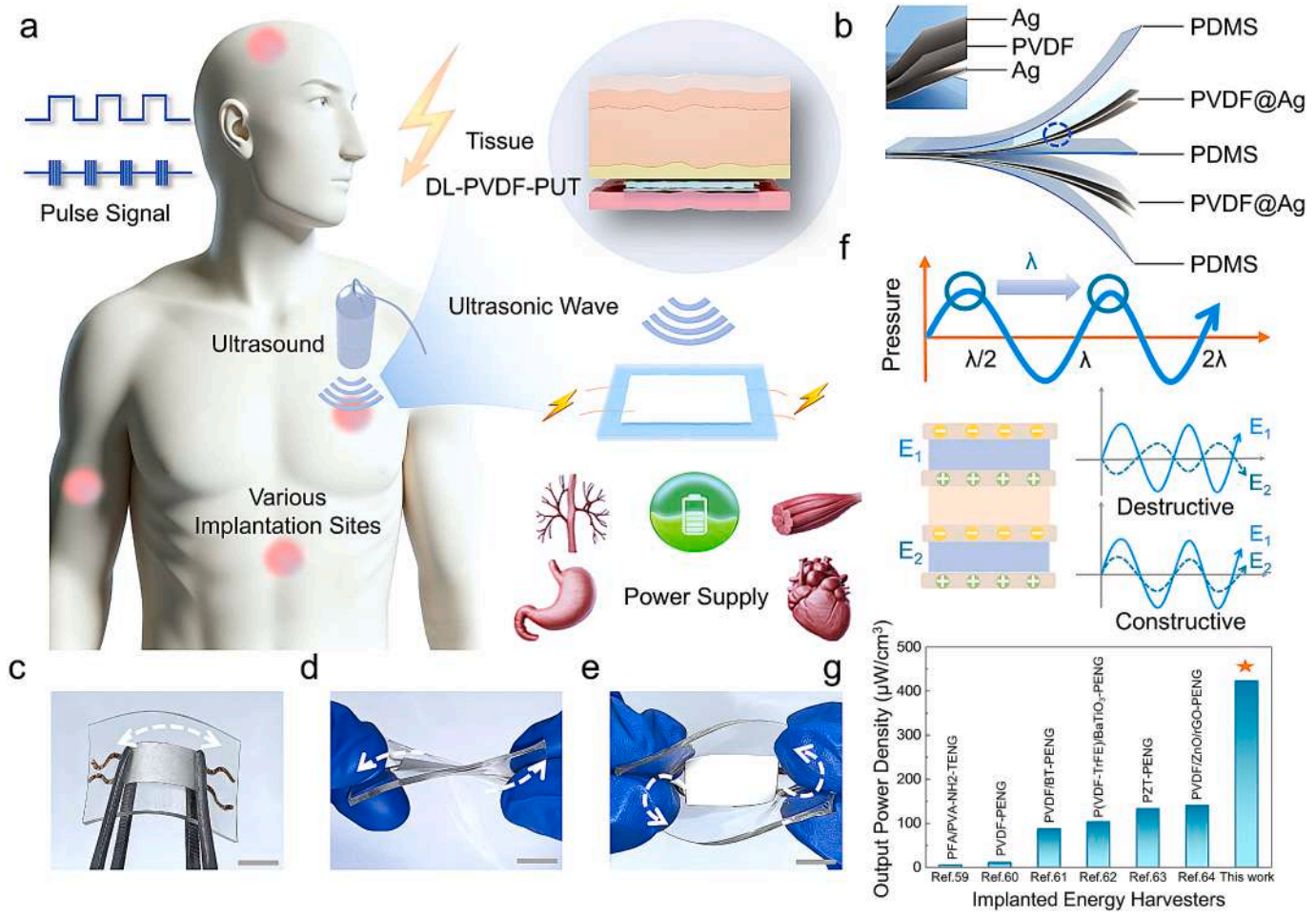


Fig. 1. Overview of the double-layer PVDF ultrasonic energy harvester for implantable wireless power supply. (a) Illustration of the harvester as an implantable bioelectronic power source driven by ultrasound at different implantation locations. (b) Structure diagram of the double-layer PVDF ultrasonic energy harvester. (c-e) Optical images of the device under different mechanical deformations, showing its flexibility and mechanical compliance (scale bars: 5 mm). (f) Schematic diagrams showing the phase-matched working principle, where interlayer-spacing regulation enables synchronized piezoelectric responses and effective potential superposition. (g) Output power density comparison between this work and other works.

layer counterpart. These findings demonstrate that the phase-matched stacking design effectively enhances the output of polymer piezoelectric transducers, providing a new structural strategy for high-performance flexible ultrasonic energy harvesters and continuous wireless powering for implantable bioelectronics.

2. Results and discussion

2.1. Design concept and working principle of the implantable ultrasonic energy harvester

Fig. 1a illustrates the application scenario of the DL-PVDF-PUT for implantable wireless power transfer. External ultrasonic waves penetrate biological tissues to directionally deliver energy to energy harvester, thereby providing a continuous power supply for implantable bioelectronics. Fig. 1b and **Fig. S1** depict the overall device architecture, which consists of outer PDMS encapsulation layers, two PVDF functional layers integrated with top and bottom Ag electrodes (as illustrated in the top-left inset), and an intervening PDMS spacer. In this configuration, adjusting the thickness of the central PDMS layer allows for the regulation of the interlayer spacing between the upper and lower PVDF functional layers, thereby controlling their phase relationship under ultrasonic excitation. When the two PVDF layers generate in-phase piezoelectric potentials, these potentials can be effectively superimposed rather than mutually cancelled, leading to an enhanced electrical output. Although the integration of advanced functionalities increases the total device thickness, the as-fabricated DL-PVDF-PUT retains decent flexibility and mechanical compliance (Fig. 1c-e), which are essential for adapting to dynamic deformations inherent to complex in vivo environments. Benefiting from the relatively low acoustic impedance of PVDF (2.7–4.0 MRayl) and PDMS (≈1.0 MRayl), which is close to that of water (~1.5 MRayl) and biological tissues (~1.5–1.7 MRayl) [47,49,58], the device achieves efficient acoustic coupling without requiring an additional matching layer. Meanwhile, to maximize the harvesting of incident ultrasonic energy while maintaining a lightweight design, no additional backing layer was introduced in this work; instead, PDMS was solely used as the encapsulation layer and to provide necessary structural support. It is worth noting that in such multilayered devices, the increase in the number of piezoelectric layers does not necessarily enhance the overall output due to signal coherence or cancellation effects. Fig. 1f further illustrates the underlying operating mechanism of the device. Given that propagating ultrasonic waves exhibit a periodic pressure distribution, the local acoustic phase is intrinsically determined by spatial position. Upon tuning the interlayer spacing to position both PVDF layers at equiphasic loci, their respective piezoelectric potentials achieve synchronization, thereby enabling constructive superposition and a marked enhancement in overall power output. In contrast, spatial deviation from this phase-matching condition induces a phase shift, causing partial cancellation of the generated piezoelectric potentials and weakened device performance. Finally, Fig. 1g and **Table S1** compare the output power density of this work with prior reports on implantable energy harvesters [59–64], demonstrating that the DL-PVDF-PUT delivers markedly higher performance. The superior output performance of our DL-PVDF-PUT validates that the phase-matched stacking strategy effectively enhances the acousto-electric conversion efficiency of polymer-based transducers.

2.2. Phase-matching mechanism and theoretical validation of the DL-PVDF-PUT

To elucidate the mechanism driving the enhanced output of the DL-PVDF-PUT, a phase-matching model was established that correlates spacer thickness, interlayer phase relationship, and electrical output. The model was subsequently verified through combined experiments and simulations. Morphologically, the device exhibits a well-defined PVDF–PDMS–PVDF laminated architecture formed by two PVDF functional layers separated by a PDMS spacer (Fig. 2a-b). The central PDMS layer provides the structural foundation for acoustic phase regulation. By tuning the thickness of this PDMS layer, the phase difference of acoustic stimulation imparted to the two PVDF films can be precisely controlled. Comprehensive material characterization (EDS, XRD, and FTIR) confirm a high fraction of electroactive β phase and robust piezoelectric activity within the PVDF layers (**Fig. S2–S4**, Supporting Information). The piezoelectric coefficient of the PVDF functional layer was measured to be approximately 31 pC/N (**Fig. S5**, Supporting Information). Because propagating ultrasonic waves exhibit a periodic phase distribution, the spacer thickness determines the relative phase excitation of the two PVDF layers. As schematically illustrated in Fig. 2c, an effective thickness of $d = \lambda$ (where d is the effective thickness and λ is the ultrasonic wavelength) aligns both PVDF layers at equivalent acoustic phase positions, where the upper and lower PVDF layers are simultaneously located at a wave crest or a wave trough. Under this condition, the piezoelectric potentials generated by the two layers exhibit the same phase and polarity, allowing them to be directly superimposed rather than cancelled, thereby yielding the maximum electrical output ($E = E_1 + E_2$, where E is the total piezoelectric potential, and E_1 and E_2 represent the potentials generated by the upper and lower PVDF layers, respectively). Conversely, when $d = \lambda/2$, the two layers experience opposite-phase acoustic excitation resulting in piezoelectric potentials with opposite phases or polarities. This causes partial cancellation of the generated potentials, and thus weakens the overall output. The required PDMS spacer thickness (d_{PDMS}) can be determined by Eq. (1),

$$d_{PDMS} = \frac{c_{PDMS}}{f}\left(N - \frac{d_{PVDF} f}{c_{PVDF}}\right) \tag{1}$$

where c_{PDMS} and c_{PVDF} are the acoustic velocities in PDMS and PVDF, respectively, d_{PVDF} is the thickness of a single PVDF layer, f is the operating frequency, and N is the wavelength-multiple factor corresponding to the targeted phase condition. It is worth noting that the proposed phase-matching strategy is not restricted to PDMS. Given that the acoustic phase delay is jointly determined by the acoustic velocity and the spacer thickness, the optimal spacer thickness can be readily redesigned for alternative elastomeric materials according to their acoustic properties. Finite-element simulations confirm that optimized spacer configurations yield comparable electrical outputs across various candidate materials, including silicone rubber, TPU, and PI (**Fig. S6** and **Table S2**, Supporting Information), demonstrating the general applicability of the proposed wavelength-based phase-matching mechanism.

To validate the phase-matching mechanism, four groups of devices with $d = \lambda/4$, $\lambda/2$, $3\lambda/4$, and λ were fabricated and tested. Under 2 MHz ultrasonic excitation, output waveforms from the top and bottom PVDF layers reveal distinctly different phase relationships depending on the spacer of $d = \lambda/2$ (Fig. 2d) and $d = \lambda$ (Fig. 2e). The enlarged view further quantifies the phase offsets (Fig. 2f). Specifically, the temporal delay between the two layers decreases from 0.16 μs at $d = \lambda/2$ to 0.03 μs at $d = \lambda$. This result confirms that tuning the spacer thickness allows the output to switch from anti-phase to in-phase excitation, which substantially reduces interlayer phase mismatch. Consequently, as shown in Fig. 2g, the total electrical output reaches a minimum near $d = \lambda/2$ and a maximum at $d = \lambda$. This transition is consistent with the evolution from opposite-phase cancellation to in-phase superposition of the generated piezoelectric potentials. Supporting waveform evolutions further corroborate this spacer-thickness-dependent trend (**Fig. S7,** Supporting Information).

Beyond experiments, multiphysics simulations were carried out to map the acoustoelectric coupling and energy partitioning. The simulated acoustic pressure distributions demonstrate that acoustic waves continue propagating downward after crossing the first interface (Fig. 2h). This dynamic process is visualized in **Video S1** (Supporting Information). Crucially, quantitative analysis reveals that

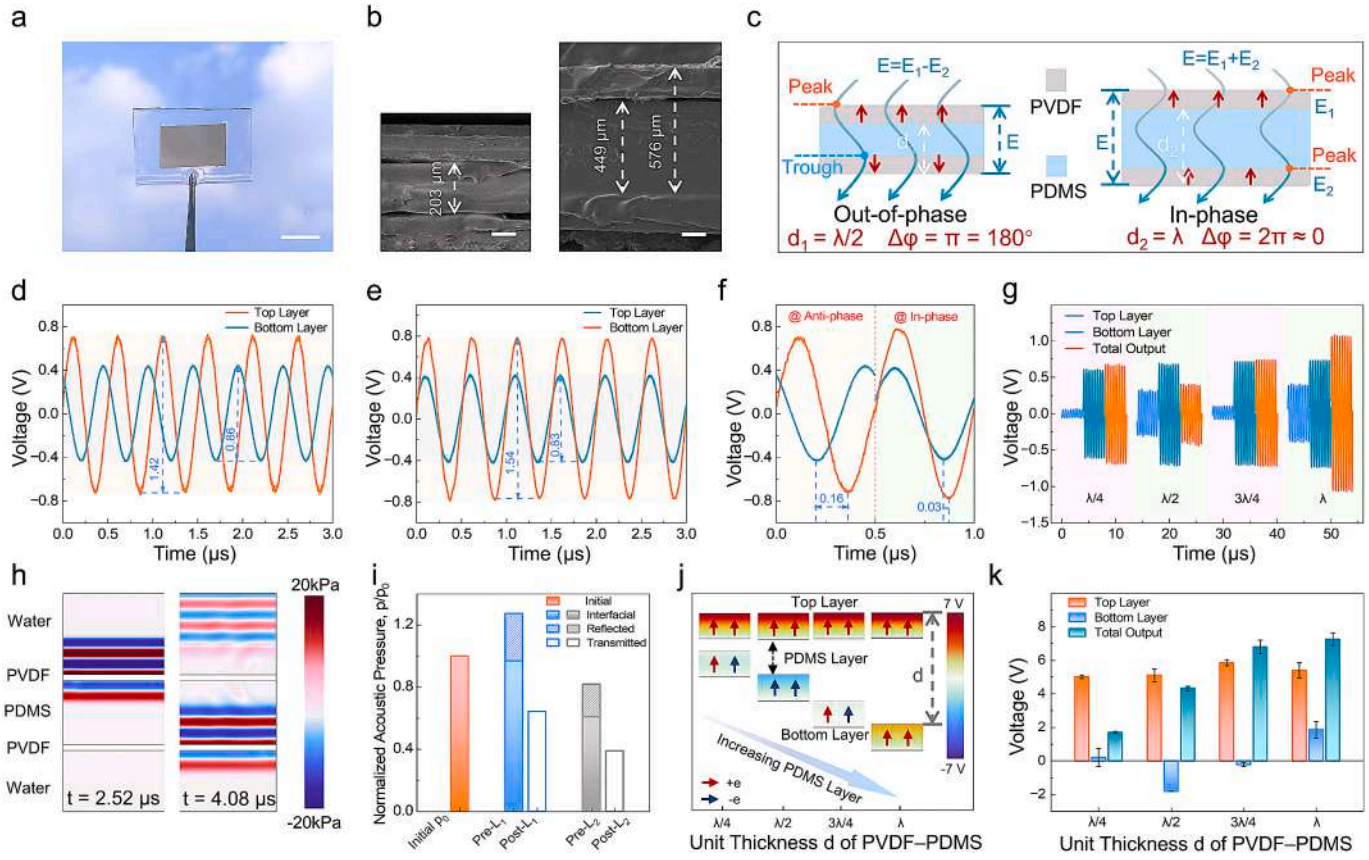


Fig. 2. Working principle and theoretical validation of the DL-PVDF-PUT. (a) Optical image of the fabricated DL-PVDF-PUT (scale bars: 10 mm). (b) Cross-sectional SEM images of the device with different spacer thicknesses (scale bars: 500 μm). (c) Phase relationship between the two PVDF functional layers under different spacer thicknesses, where $d_1 = \lambda/2$ corresponds to anti-phase output and $d_2 = \lambda$ corresponds to in-phase output. Output waveforms of the top and bottom PVDF functional layers at $d = \lambda/2$ (d) and $d = \lambda$ (e), respectively. (f) Enlarged view of the output signals. (g) Output voltages of the top layer, bottom layer, and total device under different spacer thicknesses. (h) Simulated acoustic pressure distributions across different interfaces. (i) Normalized acoustic pressure distribution with the initial pressure defined as p_0. (j) Simulated piezoelectric potential responses of the upper and lower PVDF layers under different spacer thicknesses. (k) Statistical results of the piezoelectric potential responses and total output.

approximately 64.4% of the incident acoustic energy passes through the first PVDF layer (Fig. 2i). The dual-layer design successfully captures this residual energy. Meanwhile, owing to partial acoustic reflection at the interface, the acoustic pressure measured by the probe is slightly higher than the effective acoustic pressure contributing to transmission into the device. Although partial reflections occur, the transmitted wave remains dominant and largely preserves the incident phase relationship (**Fig. S8,** Supporting Information). Simulated piezoelectric potential responses (Fig. 2j) of the two PVDF layers under different spacer thicknesses and the statistical comparison (Fig. 2k) exhibit the highest in-phase synchronization and maximum total output at $d = \lambda$. **Fig. S9** (Supporting Information) further compares the simulated total output under different spacer thicknesses, exhibiting the same trend as the experimental results, which confirms the accuracy of our phase-matching model. Collectively, these results demonstrate that rational spacer-thickness regulation enables robust acoustic phase matching and in-phase superposition of the generated piezoelectric potentials, thereby maximizing the acoustic energy harvesting capability of the stacked architecture.

2.3. *Output performance of the DL-PVDF-PUT*

The electrical characteristics of the DL-PVDF-PUT were evaluated using a custom underwater acoustic testing platform, as shown in Fig. 3a and **Fig. S10** (Supporting Information). During testing, a commercial ultrasonic transducer, driven by an amplified pulse signal, served as the acoustic excitation source, while the resulting electrical outputs from the DL-PVDF-PUT were collected and analyzed using an oscilloscope and a computer. Impedance analysis of the DL-PVDF-PUT revealed an electromechanical resonance at approximately 1.85 MHz (**Fig. S11**, Supporting Information), which is close to the designed operating frequency. Therefore, a 2 MHz ultrasonic excitation was adopted for subsequent output-performance measurements.

Under varying input driving voltages from 12 to 60 V, the output voltages of both PVDF layers exhibit a synchronized increasing trend (Fig. 3b), and the output voltages, consistent with the input excitation, display sinusoidal waveform characteristics (Fig. 3c). Crucially, the dual-layer configuration consistently outperformed its single-layer counterpart. At an input voltage of 60 V, the DL-PVDF-PUT reaches about 4.5 V, representing a 50% enhancement over the 3.0 V output of the single-layer device (Fig. 3d). Although the total output naturally attenuates as the transmission distance increases from 5 to 50 mm due to acoustic divergence, the double-layer device maintains a consistently higher output than the single-layer counterpart across the entire range (Fig. 3e). Evaluating different circuit topologies revealed that a series-connected configuration exhibits a much higher voltage output than the parallel-connected one, achieving a peak-to-peak voltage of up to 7 V at a probe-to-device distance of 5 mm (Fig. 3f). Comprehensive mapping of the performance gain (Fig. 3g) demonstrates that the phase-matched stacking strategy maintains an enhancement of over 25%, reaching up to 60% across a range of transmission distances (5 mm to 50 mm), while consistently exceeding 45% and achieving as high as 70% across varying input voltages (12 V to 60 V).

For practical implantable applications, tolerance to spatial

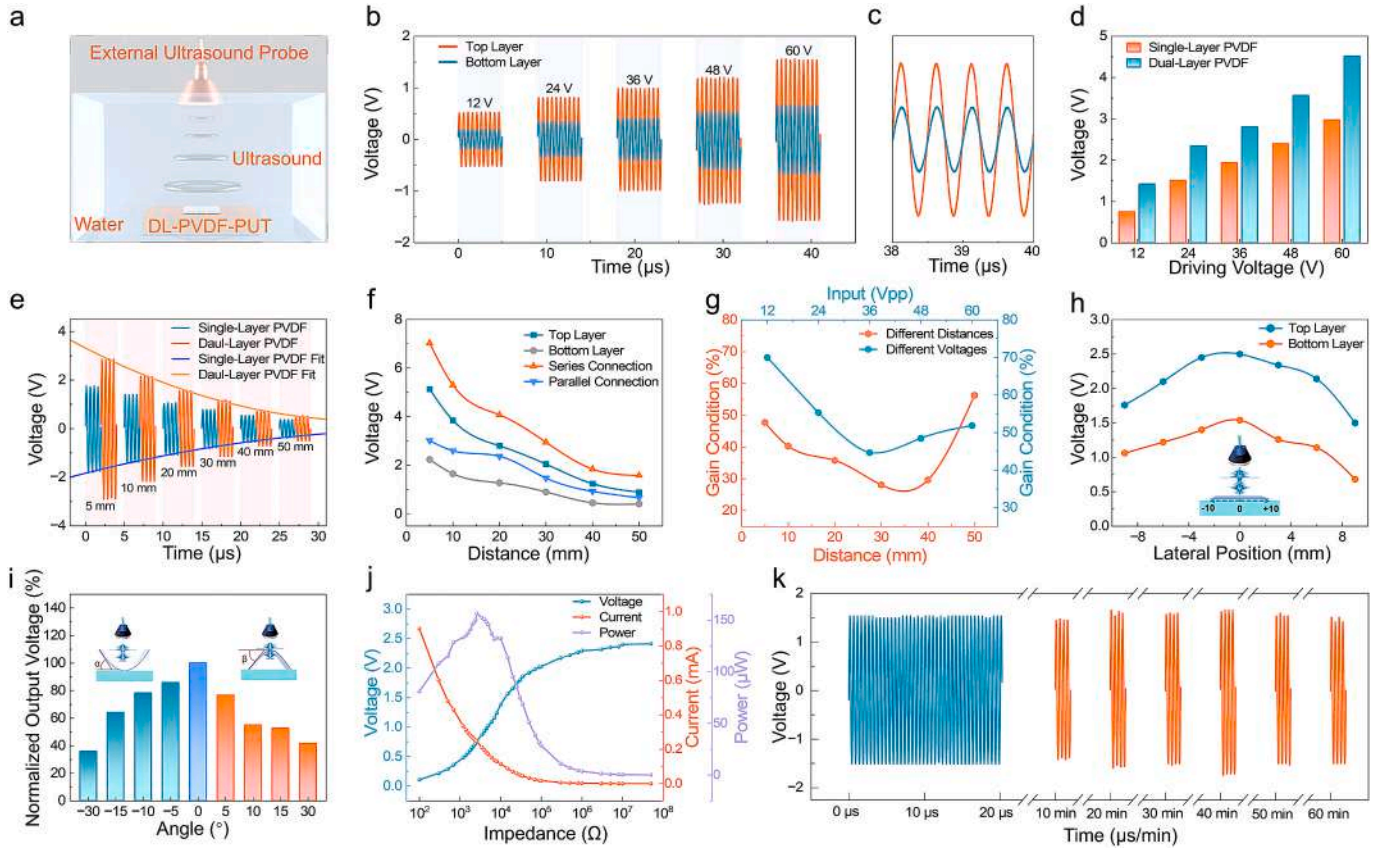


Fig. 3. Output performance of the DL-PVDF-PUT. (a) Schematic of the ultrasonic excitation and electrical measurement setup in water. (b) Layer-resolved output voltages under different input voltages. (c) Enlarged output waveform. (d) Output comparison between single-layer and dual-layer PVDF devices under different input voltages. (e) Output performance of single-layer and dual-layer devices at different transmission distances. (f) Distance-dependent outputs of the top layer, bottom layer, and the series- and parallel-connected device. (g) Effects of transmission distance and input voltage on device gain. (h) Layer-resolved outputs under different lateral excitation positions. (i) Normalized output voltage at different inclination angles. (j) Load-impedance-dependent voltage, current, and power of the device. (k) Output stability of the device during long-term operation.

misalignment and dynamic tissue deformation is critical. As shown in Fig. 3h, when the ultrasonic source is centered on the device, the outputs of the upper and lower layers are approximately 2.5 and 1.5 V, respectively. When the excitation source is laterally shifted to the edge region (10 mm left or right), the outputs decrease to about 1.5 and 0.7 V, still retaining over 50% of the initial voltage. Furthermore, the device exhibits decent mechanical stability under structural deformation. As shown in Fig. 3i, for both upward and downward bending, the device retains over 55% of its maximum output at bending angles of ±15°, and approximately 40% at ±30°. To assess the maximum energy delivery capability, load matching characterization was performed. As shown in Fig. 3j, the device achieves an optimal impedance match at a load resistance of 5 kΩ, delivering a maximum output power of 156.56 μW and a corresponding power density of 423.14 μW/cm^3. Finally, the continuous operational stability of the harvester was evaluated under long-term working conditions. As shown in Fig. 3k, an intermittent sampling method was adopted, with output signals recorded every 10 min. During continuous operation for 1 h, the output signal remained generally stable, with a variation of only approximately 10%, demonstrating that the harvester can maintain stable operation without obvious performance degradation and holds potential for long-term energy supply.

2.4. Deep-tissue power delivery capability of the DL-PVDF-PUT

To assess the practical energy-harvesting capability of the DL-PVDF-PUT for in vivo scenarios, we evaluated its performance using ex vivo porcine tissue under implantation-mimicking scenarios and explored its potential as a wireless power source for implantable cardiac electronics. Given that cardiac pacemakers typically require only microwatt-level power, with conventional systems generally consuming 10–100 μW and some leadless pacemakers operating at as low as 5–10 μW [65,66], the output power of our device (156.56 μW) indicates its potential to power such systems, as illustrated in Fig. 4a. The experimental configuration for deep implantation is shown in Fig. 4b, and a conceptual demonstration of the device for heart-rate regulation is presented in Fig. 4c. To simulate varying implantation conditions, the DL-PVDF-PUT was implanted beneath porcine tissue at depths of 5, 10 and 20 mm, corresponding to the superficial fat layer, the fat–muscle transition region, and the deeper muscle layer, respectively. The corresponding photographs and output waveforms are provided in Fig. 4d and **Fig. S12** (Supporting Information). At an implantation depth of 5 mm, the peak-to-peak output voltage exceeded 5 V (Fig. 4e). While the output inevitably attenuated with increasing tissue thickness due to intrinsic acoustic scattering and absorption, a highly detectable electrical signal was maintained even at a penetration depth of 20 mm, demonstrating its robust deep-tissue power delivery. For practical electronic integration, the generated alternating current (AC) must be rectified into direct current (DC) (Fig. 4f). Post-rectification, the output voltage reached about 2.2 V, which can drive certain low-power implantable CMOS microsystems after capacitive energy storage (with representative operating voltages of 0.6 V and 1.8 V) [10,22,67]. Furthermore, practical energy-storage capabilities were benchmarked against the single-layer counterpart. As shown in Fig. 4h, the capacitor-charging performance of the single-layer PVDF ultrasonic transducer and the DL-PVDF-PUT was compared to assess their practical energy-transfer capability.

Under identical experimental conditions, the DL-PVDF-PUT charged varying commercial capacitors (220, 470, 1000, 1500, and 2200 μF) to 2.18, 2.13, 1.98, 1.80, and 1.61 V within 15 s, respectively. Conversely, the single-layer device merely reached 1.44, 1.29, 1.23, 1.07, and 1.01 V. Notably, the harvested electrical energy was sufficient to illuminate two rows of LEDs, visually demonstrating the effective output capability of the DL-PVDF-PUT. In addition, the generated electricity was able to power a commercial electronic calculator, as shown in **Video S2** (Supporting Information). These practical demonstrations confirm the capability of the device to drive low-power electronic systems and further support its potential for powering implantable cardiac electronics, such as pacemakers. When evaluating large-scale energy-storage (**Fig. S13**, Supporting Information), the dual-layer device charged a 0.22 F supercapacitor to 0.93 V within 10 min and to 1.31 V within 20 min, vastly outperforming the 0.40 and 0.59 V reached by the single-layer device.

Comprehensive impedance analysis further confirmed the superiority of the phase-matched design under practical load conditions (Fig. 4i and **Fig. S14,** Supporting Information). The results show that the dual-layer device consistently delivers higher output voltage and power across the entire impedance range. As the load impedance increased, the output voltages of both devices gradually increased and eventually approached saturation, while the maximum output voltage of the dual-layer device reached approximately 2.01 V, representing 74.78% enhancement over the 1.15 V of the single-layer device. Maximum power transfer occurred at an optimal impedance near 5 kΩ for both devices. In particular, the peak output power of the dual-layer device was approximately 112.89 μW, yielding an 89.16% improvement compared to the single-layer device (59.68 μW). Finally, dynamic cycling tests over 10,000 on/off cycles demonstrated good operational durability (Fig. 4j and **Fig. S15**, Supporting Information). The open-circuit voltage remained stable at around 2.25 V, while the short-circuit current was maintained at about 0.542 mA, without obvious attenuation or fluctuation. Collectively, these results validate that the phase-matched stacking strategy significantly enhances the energy-conversion efficiency under realistic tissue attenuation and electrical loading, providing a promising solution for wireless powering in implantable bioelectronics.

3. Conclusion

In this work, we developed a vertically stacked ultrasonic transducer integrating double PVDF layers. By precisely regulating the interlayer spacing, we achieved constructive interference of ultrasonic waves and in-phase output of the generated piezoelectric potentials. Both experimental and simulation results demonstrated that the performance enhancement stems from physical phase synchronization rather than the mere volume accumulation of active materials. Specifically, the optimal

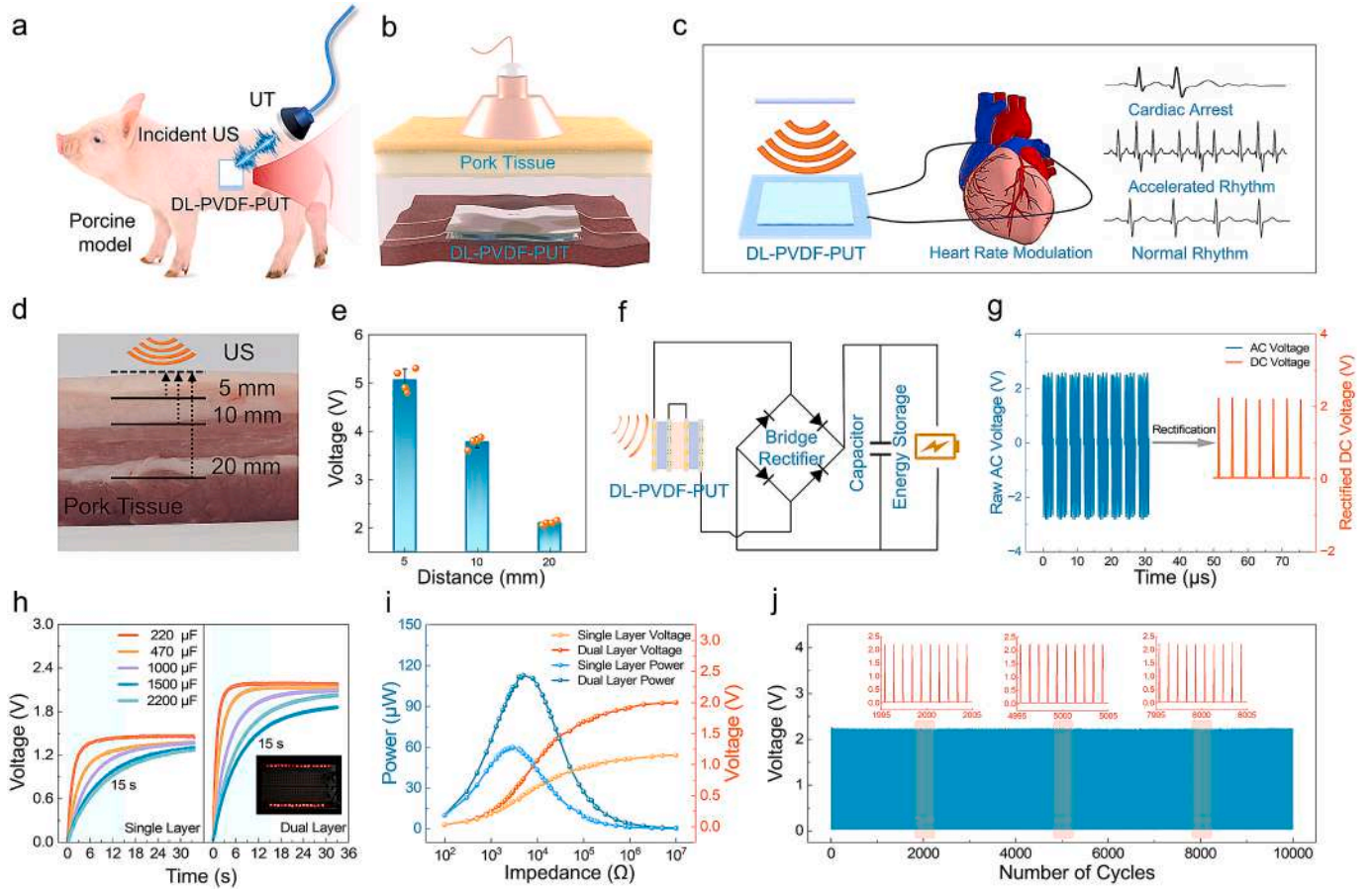


Fig. 4. Deep-tissue power delivery and application of the DL-PVDF-PUT. (a) Schematic illustration of implantable ultrasonic wireless power transfer based on a porcine model. (b) Schematic illustration of deep implantation of the DL-PVDF-PUT. (c) Conceptual demonstration of the DL-PVDF-PUT for driving a cardiac pacemaker to regulate heart rate. (d) Schematic illustration of ultrasonic transmission through porcine tissue with different thicknesses, where 5, 10, and 20 mm approximately correspond to the superficial fat layer, the fat–muscle transition region, and the deeper muscle layer, respectively. (e) Ultrasonic response of the device at the corresponding implantation depths. (f) Circuit diagram of the DL-PVDF-PUT integrated with a bridge rectifier and an energy-storage unit. (g) Output waveforms before and after rectification. (h) Charging performance comparison between single-layer and dual-layer devices under different capacitances. (i) Comparison of output voltage and power between single-layer and dual-layer devices under different load impedances. (j) Output stability of the device under repeated on/off switching.

acoustoelectric conversion occurred when the phase-matching condition satisfied $d = \lambda$. Under low-intensity ultrasonic excitation in water, the optimized DL-PVDF-PUT delivered a power density of 423.14 μW/cm^3, representing an 89.12% improvement over conventional single-layer device. Under simulated tissue conditions, the rectified output voltage reached approximately 2.2 V, enabling capacitor charging and effective load driving. Overall, this phase-matched stacking paradigm establishes a scalable structural design strategy for significantly boosting the efficiency of flexible polymeric acoustic energy harvesters, advancing sustainable wireless power solution of next-generation implantable bioelectronics.

4. Experimental section

4.1. Materials and device fabrication

Poly(vinylidene fluoride) (PVDF) films, pre-coated with silver (Ag) electrodes on both surfaces, were purchased from PolyK (USA), with a thickness of 110 μm. Polydimethylsiloxane (PDMS) was purchased from Shanghai Aladdin Biochemical Technology Co. Ltd. Silicone adhesive for interfacial bonding was obtained from Dow Corning (DOWSIL 3140). For device fabrication, the PDMS precursor and curing agent were first mixed at a mass ratio of 10:1 and stirred thoroughly, followed by degassing in a vacuum oven for 1 h to remove trapped air bubbles. The degassed PDMS was then blade-coated into films with designed thicknesses and cured on a heating plate at 80 °C for 30 min. PVDF films, PDMS films, and copper foils were cut into predefined geometries using a picosecond laser cutting system. The core functional structure was assembled into a PVDF–PDMS–PVDF sandwich configuration. The individual layers were bonded using silicone adhesive and allowed to cure naturally for 10 h. After curing, the thickness of the laminated structure was assessed by a film thickness gauge and SEM characterization. Devices exhibiting an overall thickness deviation of less than 10 μm were selected for subsequent processing. Finally, electrode leads were connected to the Ag electrode layers, using minimized copper foils as robust conductive interfaces, and the entire device was encapsulated with PDMS to obtain the double-layer flexible PVDF ultrasonic transducer (DL-PVDF-PUT). For comparison, a single-layer flexible PVDF ultrasonic transducer was fabricated following a strictly consistent protocol. Utilizing commercial PVDF films with identical specifications and geometries cut by the picosecond laser system, the single-layer device was prepared by omitting the intermediate PDMS spacer and the bottom PVDF functional layer. Subsequently, copper wires were connected to the Ag electrode layers via copper foils for electrical lead-out, and the entire device was similarly encapsulated with PDMS. Physical characterizations reveal that the fabricated DL-PVDF-PUT device, possessing an effective functional area of 10 mm × 20 mm, exhibits a total mass of merely 1.43 g and a post-encapsulation thickness of 1.85 mm (**Fig. S16**, Supporting Information).

4.2. Material characterization

The cross-sectional morphology, structural configuration, and elemental distribution of the device were characterized using scanning electron microscopy (SEM, JSM 7800F Prime) equipped with energy-dispersive X-ray spectroscopy (EDS). The crystalline phase composition of the PVDF functional layer was analyzed by X-ray diffraction (XRD, Malvern Panalytical Empyrean). Fourier-transform infrared spectroscopy (FTIR, Nicolet IS50) was further employed to evaluate the relative phase content of PVDF.

4.3. Electrical measurements

Ultrasonic excitation was generated using a function generator (AFG1062, Tektronix), a power amplifier (ATA-1220E, Aigtek), and a medical ultrasonic probe (Siemens Healthineers). The ultrasound propagated through water or biological tissue and reached the DL-PVDF-PUT, which generated AC electrical signals under ultrasonic excitation. The raw AC output signals were recorded using an oscilloscope (MDO3014, Tektronix), while the rectified DC signals were collected using an electrometer (Keithley 6517). The initial excitation signal was set to 6 Vpp, and the gain of the power amplifier was 26 dB. A schematic illustration of the overall measurement system is provided in **Fig. S10** (Supporting Information).

4.4. Finite element simulation

Finite element simulations were carried out using COMSOL Multiphysics 6.2. A two-dimensional model was adopted to represent the cross-sectional structure of the DL-PVDF-PUT, consisting of a water domain, two PVDF functional layers, and a central PDMS spacer. The thickness of each PVDF layer was set to 110 μm, while the central PDMS spacer thicknesses were set to 75, 200, 325, and 450 μm, respectively. The lateral size of the device model was set to 2 mm, corresponding to one-tenth of the length of the experimental device, and the upper and lower water domains were each set to 5 mm × 2 mm to provide sufficient acoustic propagation space. For Movie S1, the thickness of the central PDMS spacer was enlarged only for better visualization of ultrasonic propagation across different layers, while the other models were constructed according to the actual device dimensions. The coupled physics included electrostatics, solid mechanics, transient pressure acoustics, and electric circuit modules. An ultrasonic source was placed directly above the DL-PVDF-PUT model, with the initial acoustic pressure set to 200 kPa. Water was used as the surrounding medium to simulate the acoustic–electric coupling behavior of the device under ultrasonic excitation.

CRediT authorship contribution statement

Jinlong Sun: Writing – review & editing, Writing – original draft, Visualization, Validation, Supervision, Software, Resources, Project administration, Methodology, Investigation, Formal analysis, Data curation, Conceptualization. **Boling Lan:** Software, Conceptualization. **Shenglong Wang:** Formal analysis. **Hongguang Li:** Supervision. **Tianpei Xu:** Visualization. **Longchao Huang:** Methodology. **Peiwen Li:** Visualization. **Wei Zhao:** Data curation. **Yong Ao:** Data curation. **Long Jin:** Conceptualization. **Wei Zhu:** Conceptualization, Methodology, Writing – review & editing. **Weiqing Yang:** Conceptualization. **Weili Deng:** Writing – review & editing, Visualization, Supervision, Resources, Methodology, Funding acquisition, Data curation, Conceptualization.

Declaration of competing interest

The authors declare that they have no known competing financial interests or personal relationships that could have appeared to influence the work reported in this paper.

Acknowledgments

This project is supported by Beijing Key Laboratory of High-Entropy Energy materials and Devices, Beijing Institute of Nanoenergy and Nanosystems (No.GS2025MS021), the National Natural Science Foundation of China (No. U2330120) and the Fundamental Research Funds for the Central Universities (2682025CG001). We are thankful for the help from the Analysis and Testing Center of Southwest Jiaotong University.

Appendix A. Supplementary data

Supplementary data to this article can be found online at https://doi.org/10.1016/j.cej.2026.180726.

Data availability

Data will be made available on request.

References

[1] Z. Gao, Y. Zhou, J. Zhang, J. Foroughi, S. Peng, R.H. Baughman, Z.L. Wang, C. H. Wang, Advanced energy harvesters and energy storage for powering wearable and implantable medical devices, Adv. Mater. 36 (42) (2024) 2404492, https://doi.org/10.1002/adma.202404492.

[2] Y. Jo, S. Kim, J. Jeong, H.J. Lee, Ultrasound brain stimulation technologies for targeted therapeutics, Nat. Electron. 8 (8) (2025) 647–662, https://doi.org/10.1038/s41928-025-01420-3.

[3] I.M. Imani, H.S. Kim, J. Shin, D.-G. Lee, J. Park, A. Vaidya, C. Kim, J.M. Baik, Y. S. Zhang, H. Kang, S. Hur, H.-C. Song, Advanced ultrasound energy transfer technologies using metamaterial structures, Adv. Sci. 11 (31) (2024) 2401494, https://doi.org/10.1002/advs.202401494.

[4] D. Jiang, B. Shi, H. Ouyang, Y. Fan, Z.L. Wang, Z. Li, Emerging implantable energy harvesters and self-powered implantable medical electronics, ACS Nano 14 (6) (2020) 6436–6448, https://doi.org/10.1021/acsnano.9b08268.

[5] T. Liu, Y. Mao, H. Dou, W. Zhang, J. Yang, P. Wu, D. Li, X. Mu, Emerging wearable acoustic sensing technologies, Adv. Sci. 12 (6) (2025) 2408653, https://doi.org/10.1002/advs.202408653.

[6] L. Zhou, P. Liu, J. Liu, W. Yuan, Z. Wu, D. Xu, B. Hu, Y. Shao, Y. Lu, N. Huang, J. Li, Z. Li, F. Liang, X. Wu, L. Ma, M. Wang, Z. Di, R. Li, Y. Bi, F. Xu, Y. Mei, E. Song, Wireless battery-free ultrathin lithium-niobate resonator as wearable and implantable electronics for continuous monitoring of mechanical vital signs, Nat. Commun. 17 (1) (2025) 642, https://doi.org/10.1038/s41467-025-67413-0.

[7] S. Oh, J. Jekal, J. Liu, J. Kim, J.-U. Park, T. Lee, K.-I. Jang, Bioelectronic implantable devices for physiological signal recording and closed-loop neuromodulation, Adv. Funct. Mater. 34 (41) (2024) 2403562, https://doi.org/10.1002/adfm.202403562.

[8] W. Chen, X. Zheng, Y. Zhou, W. Du, F. Liang, H.-D. Yu, L. Li, Recent progress in semi-implantable bioelectronics for precision health monitoring, Adv. Funct. Mater. 35 (30) (2025) 2424463, https://doi.org/10.1002/adfm.202424463.

[9] Y. Li, N. Li, N. De Oliveira, S. Wang, Implantable bioelectronics toward long-term stability and sustainability, Matter 4 (4) (2021) 1125–1141, https://doi.org/10.1016/j.matt.2021.02.001.

[10] H. Kim, B. Rigo, G. Wong, Y.J. Lee, W.-H. Yeo, Advances in wireless, batteryless, implantable electronics for real-time, continuous physiological monitoring, Nano Micro Lett. 16 (1) (2023) 52, https://doi.org/10.1007/s40820-023-01272-6.

[11] Y. Liang, C. Zhang, R. Lin, J. Lin, J. Chen, Sustainable power solutions for next-generation medical devices, Mater. Today Bio 33 (2025) 102055, https://doi.org/10.1016/j.mtbio.2025.102055.

[12] S. Li, C. Kong, E. Wu, C. Yang, Z. Gao, X. Zhou, H. Guo, S. Jiang, J.-G. Liang, Advanced wearable biosensing and wireless integration technologies for next-generation healthcare monitoring, Soft Sci. 6 (1) (2026) 17, https://doi.org/10.20517/ss.2025.120.

[13] A. Bhatia, J. Hanna, T. Stuart, K.A. Kasper, D.M. Clausen, P. Gutruf, Wireless battery-free and fully implantable organ interfaces, Chem. Rev. 124 (5) (2024) 2205–2280, https://doi.org/10.1021/acs.chemrev.3c00425.

[14] M. Xu, Y. Liu, K. Yang, S. Li, M. Wang, J. Wang, D. Yang, M. Shkunov, S.R.P. Silva, F.A. Castro, Y. Zhao, Minimally invasive power sources for implantable electronics, Exploration 4 (1) (2024) 20220106, https://doi.org/10.1002/EXP.20220106.

[15] A. Yang, C. Tan, Y. Lin, H. Han, R. Wei, Y. Wang, K. Chen, S. Lin, L. Huang, J. Zhou, Electric field superposition for efficient implantable ultrasound energy harvesting, Chem. Eng. J. 530 (2026) 172796, https://doi.org/10.1016/j.cej.2026.172796.

[16] S.-K. Kang, R.K.J. Murphy, S.-W. Hwang, S.M. Lee, D.V. Harburg, N.A. Krueger, J. Shin, P. Gamble, H. Cheng, S. Yu, Z. Liu, J.G. McCall, M. Stephen, H. Ying, J. Kim, G. Park, R.C. Webb, C.H. Lee, S. Chung, D.S. Wie, A.D. Gujar, B. Vemulapalli, A.H. Kim, K.-M. Lee, J. Cheng, Y. Huang, S.H. Lee, P.V. Braun, W. Z. Ray, J.A. Rogers, Bioresorbable silicon electronic sensors for the brain, Nature 530 (7588) (2016) 71–76, https://doi.org/10.1038/nature16492.

[17] J. Zhang, R. Das, J. Zhao, N. Mirzai, J. Mercer, H. Heidari, Battery-free and wireless technologies for cardiovascular implantable medical devices, Adv. Mater. Technol. 7 (6) (2022) 2101086, https://doi.org/10.1002/admt.202101086.

[18] K.A. Kasper, G.F. Romero, D.L. Perez, A.M. Miller, D.A. Gonzales, J. Siqueiros, D. S. Margolis, P. Gutruf, Continuous operation of battery-free implants enables advanced fracture recovery monitoring, Sci. Adv. 11 (19) (2025) adt7488, https://doi.org/10.1126/sciadv.adt7488.

[19] H. Xue, L. Jiang, G. Lu, J. Wu, Multilevel structure engineered lead-free piezoceramics enabling breakthrough in energy harvesting performance for bioelectronics, Adv. Funct. Mater. 33 (11) (2023) 2212110, https://doi.org/10.1002/adfm.202212110.

[20] F. Mokhtari, A. Volodine, O. Deschaume, C. Bartic, A. de Kogel, X. Wang, R. J. Varley, Bioinspired flexible and stretchable coil structure from $Ti_3C_2T_x$ MXene/AgNPs-functionalized piezoelectric nanofibers for enhanced energy harvesting, Energy Environ. Mater. (2026) e70348, https://doi.org/10.1002/eem2.70348.

[21] Z. Wang, S. Zhang, J. Zeng, Z. Yin, M. Yang, Y. Liu, Z. Qin, J. Zhang, Z. Wu, X. Cui, Q. Xu, B. Zhou, W. Hu, Recent advances in self-powered implantable medical devices: energy harvesting, conversion and therapeutic applications, Rev. Mater. Res. 1 (4) (2025) 100087, https://doi.org/10.1016/j.revmat.2025.100087.

[22] Y. Zhang, P. Muthuraman, V. Andino-Pavlovsky, I. Uguz, J. Elloian, K.L. Shepard, Augmented ultrasonography with implanted CMOS electronic motes, Nat. Commun. 13 (1) (2022) 3521, https://doi.org/10.1038/s41467-022-31166-x.

[23] B.L. Turner, S. Senevirathne, K. Kilgour, D. McArt, M. Biggs, S. Menegatti, M. A. Daniele, Ultrasound-powered implants: a critical review of piezoelectric material selection and applications, Adv. Healthc. Mater. 10 (17) (2021) 2100986, https://doi.org/10.1002/adhm.202100986.

[24] J.F. Hou, M.O.G. Nayeem, K.A. Caplan, E.A. Ruesch, A. Caban-Murillo, E. Criado-Hidalgo, S.B. Ornellas, B. Williams, A.A. Pearce, H.E. Dagdeviren, M. Surets, J. A. White, M.G. Shapiro, F. Wang, S. Ramirez, C. Dagdeviren, An implantable piezoelectric ultrasound stimulator (IMPULS) for deep brain activation, Nat. Commun. 15 (1) (2024) 4601, https://doi.org/10.1038/s41467-024-48748-6.

[25] A. Cafarelli, A. Marino, L. Vannozzi, J. Puigmartí-Luis, S. Pané, G. Ciofani, L. Ricotti, Piezoelectric nanomaterials activated by ultrasound: the pathway from discovery to future clinical adoption, ACS Nano 15 (7) (2021) 11066–11086, https://doi.org/10.1021/acsnano.1c03087.

[26] S. Wang, W. Deng, H. Huang, Z. Yan, Y. Wang, T. Zhou, Y. Ao, Z. Wang, J. Zhang, G. Tian, B. Lan, Y. Sun, T. Xu, T. Yang, L. Huang, L. Jin, J. Lu, W. Yang, Strain-invariant omnidirectional stretchable MXetronics, Nat. Commun. 17 (1) (2026) 2471, https://doi.org/10.1038/s41467-026-68925-z.

[27] T. Zhang, H. Liang, Z. Wang, C. Qiu, Y.B. Peng, X. Zhu, J. Li, X. Ge, J. Xu, X. Huang, J. Tong, J. Ou-Yang, X. Yang, F. Li, B. Zhu, Piezoelectric ultrasound energy-harvesting device for deep brain stimulation and analgesia applications, Sci. Adv. 8 (15) (2022) abk0159, https://doi.org/10.1126/sciadv.abk0159.

[28] R. Hinchet, H.-J. Yoon, H. Ryu, M.-K. Kim, E.-K. Choi, D.-S. Kim, S.-W. Kim, Transcutaneous ultrasound energy harvesting using capacitive triboelectric technology, Science 365 (6452) (2019) 491–494, https://doi.org/10.1126/science.aan3997.

[29] Y. Zi, J. Wang, S. Wang, S. Li, Z. Wen, H. Guo, Z.L. Wang, Effective energy storage from a triboelectric nanogenerator, Nat. Commun. 7 (1) (2016) 10987, https://doi.org/10.1038/ncomms10987.

[30] P. Heidarian, S. Aziz, P. Halley, T. McNally, T. Peijs, L.-J. Vandi, F. Mokhtari, R. J. Varley, Self-reinforced monomaterial polyhydroxyalkanoates for sustainable packaging and piezoelectric applications, Sustain. Mater. Technol. 44 (2025) e01419, https://doi.org/10.1016/j.susmat.2025.e01419.

[31] J.V. Vidal, V. Slabov, A.L. Kholkin, M.P.S. dos Santos, Hybrid triboelectric-electromagnetic nanogenerators for mechanical energy harvesting: a review, Nano Micro Lett. 13 (1) (2021) 199, https://doi.org/10.1007/s40820-021-00713-4.

[32] B. Wang, H. Zhao, C. Jin, Y. Xu, W. Ding, Ionic-electrostatic modeling of solid-liquid triboelectric nanogenerators, Iontronics 2 (2) (2026) 17, https://doi.org/10.20517/iontronics.2026.009.

[33] D.-M. Lee, N. Rubab, I. Hyun, W. Kang, Y.-J. Kim, M. Kang, B.O. Choi, S.-W. Kim, Ultrasound-mediated triboelectric nanogenerator for powering on-demand transient electronics, Sci. Adv. 8 (1) (2022) abl8423, https://doi.org/10.1126/sciadv.abl8423.

[34] F. Xing, X. Gao, W. Gao, Y. Sun, Z. Zhao, Z.L. Wang, B. Chen, High-entropy energy for self-powered systems, SmartSys 1 (2) (2025) 70001, https://doi.org/10.1002/sys3.70001.

[35] F. Jean, M.U. Khan, A. Alazzam, B. Mohammad, Advancement in piezoelectric nanogenerators for acoustic energy harvesting, Microsyst. Nanoeng. 10 (1) (2024) 197, https://doi.org/10.1038/s41378-024-00811-4.

[36] Y. Xu, K. Zhu, E. Sun, J. Ma, Y. Li, H. Zheng, R. Zhang, B. Yang, W. Cao, Wide-bandwidth immersion ultrasound transducer made of Mn:PIMNT single crystal/epoxy 1–3 composite, Sens. Actuators A Phys. 369 (2024) 115196, https://doi.org/10.1016/j.sna.2024.115196.

[37] Q. Zhou, K.H. Lam, H. Zheng, W. Qiu, K.K. Shung, Piezoelectric single crystal ultrasonic transducers for biomedical applications, Prog. Mater. Sci. 66 (2014) 87–111, https://doi.org/10.1016/j.pmatsci.2014.06.001.

[38] S. Zhang, F. Li, X. Jiang, J. Kim, J. Luo, X. Geng, Advantages and challenges of relaxor- $PbTiO_3$ ferroelectric crystals for electroacoustic transducers a review, Prog. Mater. Sci. 68 (2015) 1–66, https://doi.org/10.1016/j.pmatsci.2014.10.002.

[39] X. Huang, R. Qian, H. Ma, D. Tang, Y. Wang, L. Jiang, J. Wu, A flexible, efficient, and fully lead-free piezoelectric ultrasound wireless energy transfer system, Adv. Funct. Mater. 36 (30) (2026) 22052, https://doi.org/10.1002/adfm.202522052.

[40] S. Chen, X. Tong, Y. Huo, S. Liu, Y. Yin, M.-L. Tan, K. Cai, W. Ji, Piezoelectric biomaterials inspired by nature for applications in biomedicine and nanotechnology, Adv. Mater. 36 (35) (2024) 2406192, https://doi.org/10.1002/adma.202406192.

[41] T. Zhang, H. Hu, H. Jiang, Z. Wang, J. Lin, Y. Cheng, W. Guo, D. Ke, H. Hang, M. Ta, J. Ou-Yang, J. Zhai, X. Yang, S. Wang, B. Zhu, KNN-based frequency-adjustable ferroelectric heterojunction and biomedical applications, Nat. Commun. 16 (1) (2025) 7120, https://doi.org/10.1038/s41467-025-62079-0.

[42] S.M. Won, L. Cai, P. Gutruf, J.A. Rogers, Wireless and battery-free technologies for neuroengineering, Nat. Biomed. Eng. 7 (4) (2023) 405–423, https://doi.org/10.1038/s41551-021-00683-3.

[43] T. Zhou, S. Wang, Y. Ao, B. Lan, Y. Sun, G. Tian, T. Yang, L. Huang, L. Jin, L. Tang, W. Yang, W. Deng, High-temperature-resistance flexible piezoelectric sensor via cyclized PAN/BTO nanofibers, Nano Energy 138 (2025) 110910, https://doi.org/10.1016/j.nanoen.2025.110910.

[44] B. Lan, C. Zhong, S. Wang, Y. Ao, Y. Liu, Y. Sun, T. Yang, G. Tian, L. Huang, J. Zhang, W. Deng, W. Yang, A highly sensitive coaxial nanofiber mask for respiratory monitoring assisted with machine learning, Adv. Fiber Mater. 6 (5) (2024) 1402–1412, https://doi.org/10.1007/s42765-024-00420-w.

[45] B. Lan, W. Deng, Y. Ao, Y. Sun, G. Tian, T. Yang, S. Wang, L. Huang, T. Zhou, P. Li, Z. Wang, T. Xu, G. Liu, J. Sun, H. Li, L. Jin, B. Zhang, F. Chun, W. Yang, Hollow-structured piezoelectric acoustic electronics for omnidirectional 3D sound capture,

Nano Energy 156 (2026) 112122, https://doi.org/10.1016/j.nanoen.2026.112122.
[46] J. Liu, G. Tian, W. Yang, W. Deng, Recent progress in flexible piezoelectric devices toward human-machine interactions, Soft Sci. 2 (4) (2022) 22, https://doi.org/10.20517/ss.2022.23.
[47] P.L.M.J. van Neer, L.C.J.M. Peters, R.G.F.A. Verbeek, B. Peeters, G. de Haas, L. Hörchens, L. Fillinger, T. Schrama, E.J.W. Merks-Swolfs, K. Gijsbertse, A.E.C. M. Saris, M. Mozaffarzadeh, J.M. Menssen, C.L. de Korte, J.-L.P.J. van der Steen, A. W.F. Volker, G.H. Gelinck, Flexible large-area ultrasound arrays for medical applications made using embossed polymer structures, Nat. Commun. 15 (1) (2024) 2802, https://doi.org/10.1038/s41467-024-47074-1.
[48] T. Xu, L. Jin, Y. Ao, J. Zhang, Y. Sun, S. Wang, Y. Qu, L. Huang, T. Yang, W. Deng, W. Yang, All-polymer piezo-ionic-electric electronics, Nat. Commun. 15 (1) (2024) 10876, https://doi.org/10.1038/s41467-024-55177-y.
[49] K. Keller, C. Leitner, C. Baumgartner, L. Benini, F. Greco, Fully printed flexible ultrasound transducer for medical applications, Adv. Mater. Technol. 8 (18) (2023) 2300577, https://doi.org/10.1002/admt.202300577.
[50] C. Ning, S. Xiang, X. Sun, X. Zhao, C. Wei, L. Li, G. Zheng, K. Dong, Highly stretchable kirigami-patterned nanofiber-based nanogenerators for harvesting human motion energy to power wearable electronics, Mater. Futures 3 (2) (2024) 025101, https://doi.org/10.1088/2752-5724/ad2f6a.
[51] G. Tian, W. Deng, D. Xiong, T. Yang, B. Zhang, X. Ren, B. Lan, S. Zhong, L. Jin, H. Zhang, L. Deng, W. Yang, Dielectric micro-capacitance for enhancing piezoelectricity via aligning MXene sheets in composites, Cell Rep. Phys. Sci. 3 (4) (2022) 100814, https://doi.org/10.1016/j.xcrp.2022.100814.
[52] J. Li, Y. Ma, T. Zhang, K.K. Shung, B. Zhu, Recent advancements in ultrasound transducer: from material strategies to biomedical applications, BME Front. 2022 (2022) 9764501, https://doi.org/10.34133/2022/9764501.
[53] T. Yang, W. Deng, X. Chen, Q. Wang, G. Tian, Y. Sun, S. Wang, D. Xiong, J. Song, L. Huang, B. Wu, B. Zhang, B. Lan, L. Jin, W. Yang, Q. Wang, Topological structure-induced piezoelectricity from the α-phase poly(vinylidene fluoride), Adv. Mater. 38 (7) (2026) 18326, https://doi.org/10.1002/adma.202518326.
[54] B. Chen, Z. Feng, F.-Z. Yao, M.-H. Zhang, K. Wang, Y. Wei, W. Gong, J. Rödel, Flexible piezoelectrics: integration of sensing, actuating and energy harvesting, NPJ Flexible Electron. 9 (1) (2025) 58, https://doi.org/10.1038/s41528-025-00432-5.
[55] Z. Zhang, Z. Wang, X. Li, Y. Zheng, Z. Yang, Design and manufacturing of piezoelectric biomaterials for bioelectronics and biomedical applications, Chem. Rev. 125 (20) (2025) 9875–9929, https://doi.org/10.1021/acs.chemrev.5c00399.
[56] Y. Ao, L. Jin, S. Wang, B. Lan, G. Tian, T. Xu, L. Huang, Z. Wang, Y. Sun, T. Yang, W. Deng, F. Yang, W. Yang, Dual structure reinforces interfacial polarized MXene/PVDF-TrFE piezoelectric nanocomposite for pressure monitoring, Nano Micro Lett. 17 (1) (2025) 320, https://doi.org/10.1007/s40820-025-01839-5.
[57] Y. Ao, T. Yang, G. Tian, S. Wang, T. Xu, L. Deng, J. Zhang, L. Tang, W. Deng, L. Jin, W. Yang, Tertiary orientation structures enhance the piezoelectricity of MXene/PVDF nanocomposite, Nano Res. 17 (6) (2024) 5629–5635, https://doi.org/10.1007/s12274-023-6418-7.
[58] C. Qiu, Z. Zhang, Z. Xu, L. Qiao, L. Ning, S. Zhang, M. Su, W. Wu, K. Song, Z. Xu, L.-Q. Chen, H. Zheng, C. Liu, W. Qiu, F. Li, Transparent ultrasonic transducers based on relaxor ferroelectric crystals for advanced photoacoustic imaging, Nat. Commun. 15 (1) (2024) 10580, https://doi.org/10.1038/s41467-024-55032-0.
[59] H. Ryu, H.-M. Park, M.-K. Kim, B. Kim, H.S. Myoung, T.Y. Kim, H.-J. Yoon, S. S. Kwak, J. Kim, T.H. Hwang, E.-K. Choi, S.-W. Kim, Self-rechargeable cardiac pacemaker system with triboelectric nanogenerators, Nat. Commun. 12 (1) (2021) 4374, https://doi.org/10.1038/s41467-021-24417-w.
[60] Y.-K. Fuh, J.-C. Ye, P.-C. Chen, H.-C. Ho, Z.-M. Huang, Hybrid energy harvester consisting of piezoelectric fibers with largely enhanced 20 V for wearable and muscle-driven applications, ACS Appl. Mater. Interfaces 7 (31) (2015) 16923–16931, https://doi.org/10.1021/acsami.5b03955.
[61] F. Mokhtari, G.M. Spinks, C. Fay, Z. Cheng, R. Raad, J. Xi, J. Foroughi, Wearable electronic textiles from nanostructured piezoelectric fibers, Adv. Mater. Technol. 5 (4) (2020) 1900900, https://doi.org/10.1002/admt.201900900.
[62] C.K. Jeong, C. Baek, A.I. Kingon, K.-I. Park, S.-H. Kim, Lead-free perovskite nanowire-employed piezopolymer for highly efficient flexible nanocomposite energy harvester, Small 14 (19) (2018) 1704022, https://doi.org/10.1002/smll.201704022.
[63] J. Le Scornec, B. Guiffard, R. Seveno, V. Le Cam, Frequency tunable, flexible and low cost piezoelectric micro-generator for energy harvesting, Sens. Actuators A Phys. 312 (2020) 112148, https://doi.org/10.1016/j.sna.2020.112148.
[64] S. Azimi, A. Golabchi, A. Nekookar, S. Rabbani, M.H. Amiri, K. Asadi, M. M. Abolhasani, Self-powered cardiac pacemaker by piezoelectric polymer nanogenerator implant, Nano Energy 83 (2021) 105781, https://doi.org/10.1016/j.nanoen.2021.105781.
[65] A. Zurbuchen, A. Haeberlin, L. Bereuter, J. Wagner, A. Pfenniger, S. Omari, J. Schaerer, F. Jutzi, C. Huber, J. Fuhrer, R. Vogel, The Swiss approach for a heartbeat-driven lead- and batteryless pacemaker, Heart Rhythm. 14 (2) (2017) 294–299, https://doi.org/10.1016/j.hrthm.2016.10.016.
[66] L. Bereuter, M. Gysin, T. Kueffer, M. Kucera, T. Niederhauser, J. Fuhrer, P. Heinisch, A. Zurbuchen, D. Obrist, H. Tanner, A. Haeberlin, Leadless dual-chamber pacing: a novel communication method for wireless pacemaker synchronization, JACC Basic Transl. Sci. 3 (6) (2018) 813–823, https://doi.org/10.1016/j.jacbts.2018.07.009.
[67] I. Habibagahi, J. Jang, A. Babakhani, Miniaturized wirelessly powered and controlled implants for multisite stimulation, IEEE Trans. Microw. Theory Tech. 71 (5) (2023) 1911–1922, https://doi.org/10.1109/tmtt.2022.3233368.